Journal of Advanced Ceramics
2019, **8**(4): 537–544
https://doi.org/10.1007/s40145-019-0336-2
ISSN 2226-4108
CN 10-1154/TQ

Research Article

Influence of HfO_2 alloying effect on microstructure and thermal conductivity of $HoTaO_4$ ceramics

Lin CHEN, Jing FENG*

Faculty of Material Science and Engineering, Kunming University of Science and Technology, Kunming 650093, China

Received: March 25, 2019; Revised: April 22, 2019; Accepted: April 23, 2019

Abstract: HfO_2 alloying effect has been applied to optimize thermal insulation performance of $HoTaO_4$ ceramics. X-ray diffraction, Raman spectroscopy, and X-ray photoelectron spectroscopy are employed to decide the crystal structure. Scanning electronic microscopy is utilized to detect the influence of HfO_2 alloying effect on microstructure. Current paper indicates that the same numbers of Ta^{5+} and Ho^{3+} ions of $HoTaO_4$ are substituted by Hf^{4+} cations, and it is defined as alloying effect. No crystal structural transition is introduced by HfO_2 alloying effect, and circular pores are produced in $HoTaO_4$. HfO_2 alloying effect is efficient in decreasing thermal conductivity of $HoTaO_4$ and it is contributed to the differences of ionic radius and atomic weight between Hf^{4+} ions and host cations (Ta^{5+} and Ho^{3+}). The least experimental thermal conductivity is 0.8 $W \cdot K^{-1} \cdot m^{-1}$ at 900 ℃, which is detected in 6 and 9 mol%-HfO_2 $HoTaO_4$ ceramics. The results imply that HfO_2–$HoTaO_4$ ceramics are promising thermal barrier coatings (TBCs) due to their extraordinary thermal insulation performance.

Keywords: thermal barrier coating (TBC); thermal conductivity; rare earth tantalates; microstructure; alloying effect; optical property

1 Introduction

Thermal barrier coating (TBC) system, which is applied in multiple gas turbines and aircraft engines, is consist of top coat ceramics, bond coat, and super-alloy substrates [1–5]. As the limit application temperature of present Ni-based alloy is less than 1200 ℃, a great number of researchers are studying top coat ceramics to provide thermal insulation [6–9]. The main functions of top coat ceramics are to decrease superficial temperature of substrates and increase their application limitations. Current top coat ceramics are yttria stabilized zirconia (YSZ), whose working temperature is less than 1200 ℃. The t–m phase transition is detected in YSZ, and the unit cell volume variation caused by the transition will lead to the failure of coatings [10–12]. Nevertheless, no material is able to replace YSZ because the distinctive ferroelasticity produces excellent toughness at elevated temperature [13]. Therefore, much effort has been conducted to perfect the thermal physical performance of YSZ [12–15]. At the same time, substances exhibiting ferroelasticity are recognized as novel TBCs. Monoclinic ABO_4-type rare earth tantalates (m-$RETaO_4$) possess the similar ferroelasticity, which engenders extraordinary toughness [16–18]. Herein, m-$RETaO_4$ has been widely deliberated as candidate TBC materials. Preceding documents reveal that m-$RETaO_4$ displays outstanding thermal insulation performance

* Corresponding author.
E-mail: jingfeng@kust.edu.cn

(k = 1.5 $W \cdot K^{-1} \cdot m^{-1}$), and the typical microstructure has been researched [16,18]. The comprehensive properties of m-$RETaO_4$ are better than that of YSZ and other candidate TBCs ($RE_2Zr_2O_7$, RE_3TaO_7, $REPO_4$, and so on) [19–23]. To promote the material property of rare earth tantalates further, many methods have been tried. For example, TiO_2 and ZrO_2 alloying effects are employed to produce glass-like thermal conductivity; Al_2O_3 doping is utilized to drop thermal conductivity and enhance thermal expansion coefficients (TECs) [19,24,25]. Among various technologies, alloying effect is considered as the most effective one, as the TECs and thermal conductivity are simultaneously optimized. $HoTaO_4$ exhibits the best thermal radiation resistance, low Young's modulus, and thermal conductivity, as well as high TECs in the whole series of m-$RETaO_4$ [18]. TiO_2 and ZrO_2 alloying effects have been tried for other rare earth tantalates, as Hf, Zr, and Ti belong to the same group, HfO_2 alloying effect is tried for $HoTaO_4$.

In this paper, HfO_2 alloying $HoTaO_4$ sample had been composed through a conventional solid-state reaction. X-ray diffraction (XRD) was applied to investigate the crystal structure. Raman spectroscopy was used to appraise the molecule vibration intensity. X-ray photoelectron spectroscopy (XPS) was utilized to ascertain the chemical valence of multiple elements. Scanning electron microscopy (SEM) was employed to research the effect of HfO_2 addition on the microstructure of $HoTaO_4$ ceramics. Optical properties were thoroughly discussed. Thermal properties (specific heat, thermal diffusivity, and thermal conductivity) of HfO_2–$HoTaO_4$ were the emphasis. It is stressed that HfO_2 alloying effect is effective in optimizing thermal insulation performance of $HoTaO_4$ ceramics.

2 Experimental procedure

2. 1 Sample preparation

Bulk x mol%-HfO_2 $HoTaO_4$ (x = 0, 3, 6, 9) sample was composed through a solid-state reaction technique. The raw substances comprised Ho_2O_3 (net content ⩾ 99.99%, pellet diameter ⩽ 3 μm), Ta_2O_5 (net content ⩾ 99.99%, pellet diameter ⩽ 5 μm), HfO_2 (net content ⩾ 99.99%, pellet diameter ⩽ 5 μm), and C_2OH_6 (net content ⩾ 99.9%). Ho_2O_3, Ta_2O_5, and HfO_2 were mixed in a ball crusher (10 h, 320 r/min) within circumstance of C_2OH_6. The admixtures were kept at 105 ℃ for 8 h to season. The acquired substances were suppressed into columns of 7.5 mm in radius and 2 mm in altitude. Ultimately, the columns were placed at 1700 ℃ for 10 h to synthesize circular x mol%-HfO_2 $HoTaO_4$ specimens.

2. 2 Crystal structure identification and microstructure observation

The lattice structures were distinguished through XRD (Rigaku, MiniFlex600, Japan). The 2-theta degree stretched from 10° to 70°, when the scanning velocity was 6 (°)/min and the step length was 0.02°. Herein, the testing time of each sample XRD pattern continued about 10 min. Archimedes principle was utilized to obtain the bulk density (ρ), and the porosity was computed by the relationship:

$$\phi = 1 - \rho / \rho_0 \tag{1}$$

Raman spectroscopy was more sensitive on distinguishing crystal structure variation than XRD, and it was used to research the vibration variety of unit cell and multiple chemical bonds. Confocal spectrometer (Lab RAM Aramis, Horiba-Jobin Yvon, Edison, NJ, USA) possessing a He–Ne ion laser (514.5 nm) was employed to record the Raman result. XPS was carried out within a PHI 5000 Versaprobe-II spectrometer. The specimen was burnished and was wiped to clear up any foreign pollutant. A carbon layer with C1s binding energy of 284.8 eV was coated to eliminate the experimental deviation originating from superficial charging effect.

SEM (JEOL, JSM-7001F, Tokyo, Japan) was used to survey the superficial morphology features including pores, cracks, and grain sizes, which were evidently affected by HfO_2 alloying effect. Before the observation, gold was coated on the surface to increase electrical conductivity; the resulting images with magnification of 500 and 1000 were displayed.

2. 3 Property measurement

The band gap of x mol%-HfO_2 $HoTaO_4$ was calculated based on reflectance R, which was measured via one UV–vis spectrophotometer (Shimadzu UV-3600plus, Japan). The reflectance curves were obtained, and the band gaps were computed according to the K–M law [26]:

$$F(R) = \frac{(1-R)^2}{2R} \tag{2}$$

where $F(R)$ exhibited a close relationship with the extinction efficiency (φ).

Thermal diffusivity (α) experiment was completed

in a laser flash instrument (LFA 457, Netzsch, Germany) from 25 to 900 ℃. The experimental values were revised via Radiation+Pulse adjustment mold. The thermal conductivity was calculated based on α, C_p, and ρ [27]:

$$k' = \alpha C_p \rho \tag{3}$$

Specific heat (C_p) was gained by Neumann–Kopp law [30]. Pores and cracks usually produced an obvious impact on heat propagation; the thermal conductivity (k) of specimen without pores and cracks was [27]:

$$\frac{k'}{k} = 1 - \frac{4}{3}\phi \tag{4}$$

3 Results and discussion

3. 1 Crystal structure

Figure 1(a) displays that XRD peaks of x mol%-HfO_2 $HoTaO_4$ (x = 0, 3, 6, 9) are in accordance with the patterns of PDF#24-0478, implying that each sample crystallizes in m phase, and no phase transformation has been detected. According to the ionic radius of Ho^{3+} (r = 0.102 nm), Ta^{5+} (r = 0.064 nm), and Hf^{4+} (r = 0.083 nm) cations, when only Ta^{5+} is substituted by Hf^{4+} or Hf^{4+} occurs as interstitial cation, the crystal structure will be expanded and the XRD peaks shift to left. When Ho^{3+} is substituted by Hf^{4+}, the crystal structure will be contracted, and the XRD peaks shift to right. Figure 1(b) indicates that the 2-theta position of main XRD peaks of HfO_2–$HoTaO_4$ is constant; therefore, it is believed that the same numbers of Ho^{3+} and Ta^{5+} ions are substituted by Hf^{4+} cations [19,24]. A weak peak of HfO_2 is found in 9 mol%-HfO_2 $HoTaO_4$, which can be observed more distinctly from Fig. 1(c), proving that HfO_2 alloying content in $HoTaO_4$ is below 9 mol%. Figure 2(a) displays that the entire series of x mol%-HfO_2 $HoTaO_4$ ceramics present analogous Raman peaks; no Raman peak position shifting is discovered. The position and intensity of Raman peaks are close to the chemical bonds length and lattice vibration strength. Figures 2(b) and 2(c) imply that no palpable change of crystal structure and bonding length is introduced by HfO_2 alloying effect. Figure 3(a) displays that Hf, Ho, Ta, O, and C elements are found in 6 mol%-HfO_2 $HoTaO_4$ ceramics according to the binding energy. The element chemical valence can be determined based on the binding energy shown in Figs. 3(b)–3(e) [29,30]. For example, the binding energy of O^{2-} is 295.5 eV,

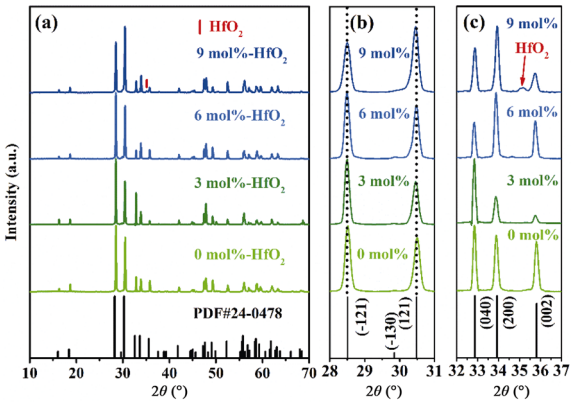

Fig. 1 Room temperature XRD patterns of x mol%-HfO_2 $HoTaO_4$ (x = 0, 3, 6, 9) ceramics: (a) 10° ⩽ 2θ ⩽ 70°, (b) 28° ⩽ 2θ ⩽ 31°, (c) 32° ⩽ 2θ ⩽ 37°.

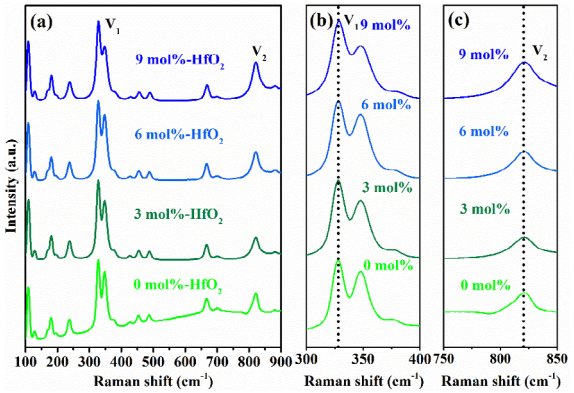

Fig. 2 Room temperature Raman spectra of x mol%-HfO_2 $HoTaO_4$ (x = 0, 3, 6, 9) ceramics: (a) 100–900 cm^{-1}, (b) 300–400 cm^{-1}, (c) 750–850 cm^{-1}.

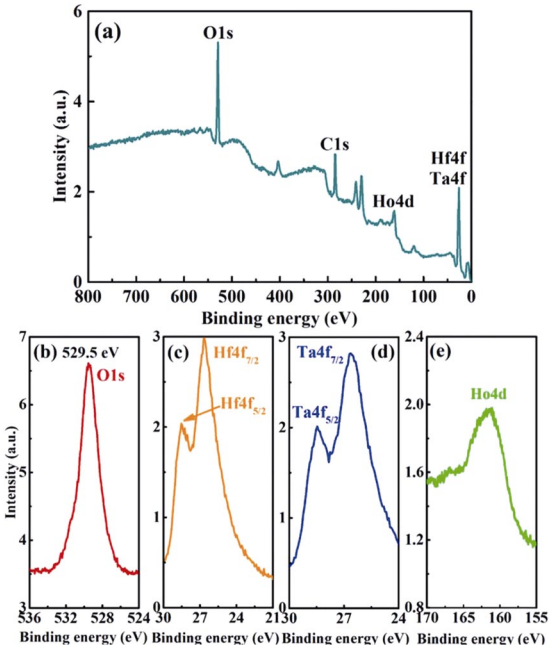

Fig. 3 XPS results of 6 mol%-HfO_2 $HoTaO_4$ ceramics.

indicating that O is combined with metal elements (Ta^{5+}, Hf^{4+}, Ho^{3+}) to form chemical bonds.

3. 2 Microstructure

The grain size of 0 mol%-HfO_2 $HoTaO_4$ is small ($\leqslant$ 20 μm) as displayed in Fig. 4, which is analogous to the former document [18]. In $HoTaO_4$, a small quantity of pore and crack is observed, and the relative density is about 95%. However, when HfO_2 is added, a large number of columnar pores are emerged as shown in Figs. 4(c)–4(h). The grain size of x mol%-HfO_2 $HoTaO_4$ (x = 3, 6, 9) is bigger than that of $HoTaO_4$, as it can be clearly observed from Figs. 4(d), 4(f), and 4(h). Some grains are much bigger than 20 μm, and the grain boundaries are blurry, which are caused by the addition of HfO_2. The exact density and porosity of x mol%-HfO_2 $HoTaO_4$ are listed in Table 1. The porosity increases with increment of HfO_2 content, and the porosity of $HoTaO_4$ can be regulated via controlling HfO_2 content. Normally, the porosity of TBCs is about 10% [27,31,32]. Therefore, the realistic thermal and mechanical properties of $HoTaO_4$ coatings can be estimated by adding appropriate HfO_2 content to obtain the desirable porosity.

3. 3 Optical properties

Figure 5(a) displays that the reflectance of x mol%-HfO_2 $HoTaO_4$ increases with increment of wavelength, and periodic decrements of reflectance are presented in some specific positions, which are caused by the Ho^{3+} internal $4f^{11}$ transition [33]. Figure 5(b) displays that the absorption decreases with increment of wavelength, which is contrary to the situation of reflectance, and the maximum absorption reaches 63% between 100 and 200 nm of wavelength range. Figure 5(c) displays that the band gaps of x mol%-HfO_2 $HoTaO_4$ (x = 0, 3, 6) are similar, whereas 9 mol%-HfO_2 $HoTaO_4$ exhibits narrower band gap than the others, attributed to the existence of second phase HfO_2. The wide band gap of x mol%-HfO_2 $HoTaO_4$ proves that they are insulators and heat is carried by phonons (lattice vibration) in these solids.

3. 4 Thermal conductivity

Figure 6(a) displays that the specific heat (0.30–0.39 $J{\cdot}K^{-1}{\cdot}g^{-1}$, 25–900 ℃) of x mol%-HfO_2 $HoTaO_4$ increases with increment of temperature, contributed to the volume bulge and phonon excitation [17,21]. The introduction of HfO_2 makes little impact on the specific heat of $HoTaO_4$. Figure 6(b) displays that thermal diffusivity (0.31–1.37 mm^2/s, 25–900 ℃) decreases with increment of HfO_2 quantity, and the least value is presented in 6 and 9 mol%-HfO_2 $HoTaO_4$. Figure 6(c) displays that thermal conductivity (0.8–3.6 $W{\cdot}K^{-1}{\cdot}m^{-1}$, 25–900 ℃) decreases with increment of temperature. The difference of thermal conductivity k' among x mol%-HfO_2 $HoTaO_4$ is much higher than that of the revised thermal conductivity k as shown in Figs. 6(c) and 6(d), because circular pores are effective in scattering phonons and reducing thermal conductivity. The minimum k reaches 1.3 $W{\cdot}K^{-1}{\cdot}m^{-1}$ (6 mol%-HfO_2 $HoTaO_4$), which is much less than that of YSZ (2.5–3.0 $W{\cdot}K^{-1}{\cdot}m^{-1}$), $La_2Zr_2O_7$ (1.8–3.2 $W{\cdot}K^{-1}{\cdot}m^{-1}$), and other ceramics [29,31,34,35]. The low thermal conductivity of x mol%-HfO_2 $HoTaO_4$ derives from the complicated crystal structure and point defects engendered by HfO_2 alloying effect. In the crystal structure of $HoTaO_4$, each Ta^{5+} is surrounded by four O^{2-} ions to form cage-like tetrahedron, which

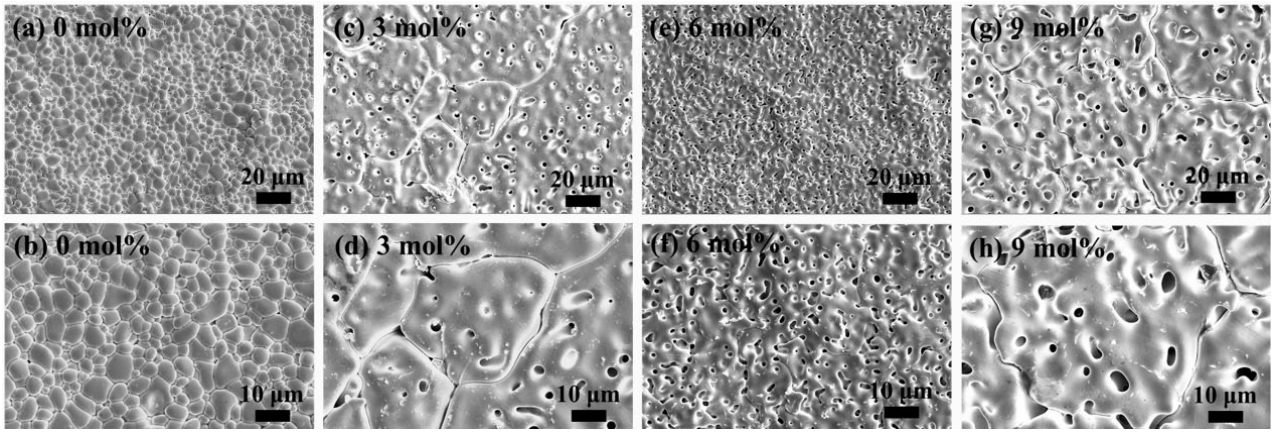

Fig. 4 Typical microstructure of x mol%-HfO_2 $HoTaO_4$ (x = 0, 3, 6, 9) ceramics.

Table 1 Density and porosity of x mol%-HfO_2 $HoTaO_4$ (x = 0, 3, 6, 9) ceramics (the theoretical density of $HoTaO_4$ is 9.277 g/cm^3)

x (mol%)	0	3	6	9
Density (g/cm^3)	8.764	7.159	6.676	6.495
Porosity (%)	5.5	22.3	28.0	29.6

leads to violent phonons scatter. Hf^{4+} has longer ionic radius than Ta^{5+} and possesses shorter ionic radius than Ho^{4+}. The misfits of ionic radius and atomic weight among Ta^{5+}, Ho^{3+}, and Hf^{4+} induce point defects and enhance phonon scattering intensity [19,36].

Figure 6(d) shows that the revised thermal conductivity k (1.3–3.7 W·K^{-1}·m^{-1}, 25–900 ℃) decreases with increment of temperature. The phonon scattering intensity introduced by point defects and grain boundary is constant; the temperature dependent thermal conductivity is governed by inharmonic lattice vibration [37–40]. Raman characteristic peaks come from the particular vibration of lattice structure and chemical bonds, and the mean full wave at half maximum (FWHM) of Raman peaks can be used to assess anharmonicity of lattice vibration. Figure 7 displays that the anharmonicity of lattice vibration of x mol%-HfO_2 $HoTaO_4$ increases

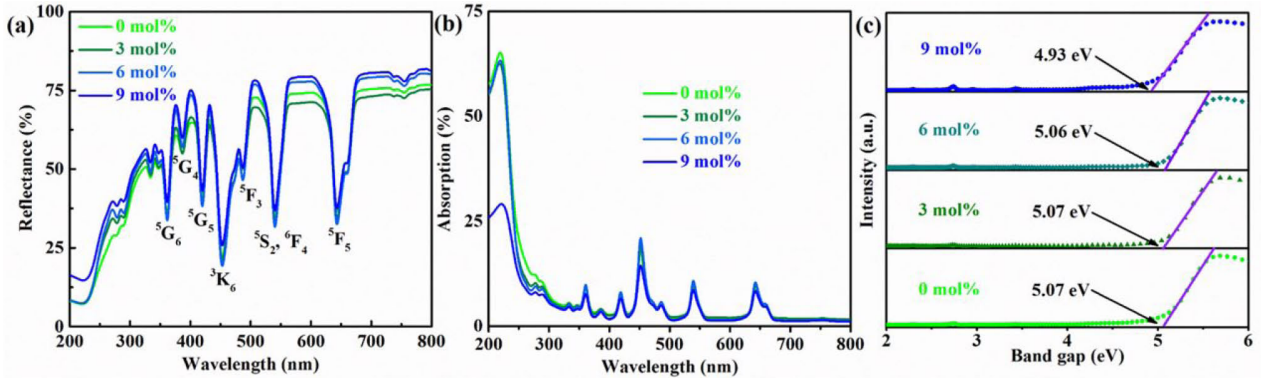

Fig. 5 Optical properties of x mol%-HfO_2 $HoTaO_4$ (x = 0, 3, 6, 9) ceramics: (a) reflectance, (b) absorption, (c) band gap.

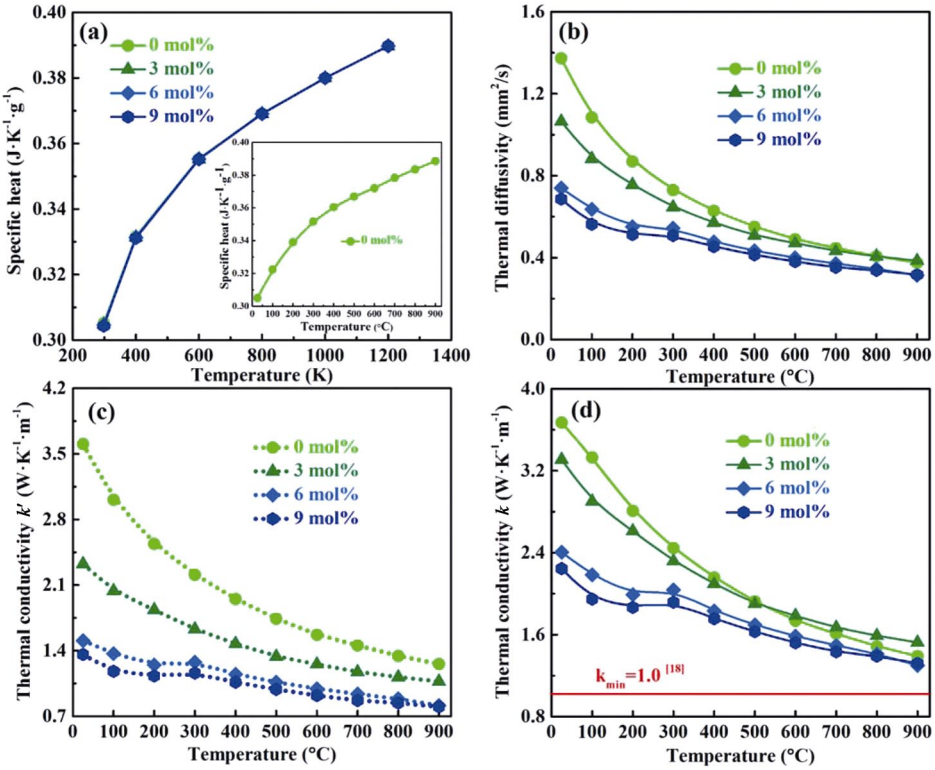

Fig. 6 Temperature dependence of thermal properties of x mol%-HfO_2 $HoTaO_4$ (x = 0, 3, 6, 9) ceramics: (a) specific heat, (b) thermal diffusivity, (c) thermal conductivity k', (d) revised thermal conductivity k.

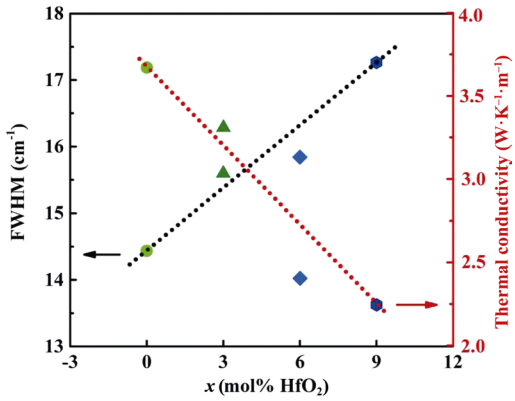

Fig. 7 Composition dependence of the revised thermal conductivity k at room temperature and the mean full wave at half maximum (FWHM) of Raman peaks of x mol%-HfO_2 $HoTaO_4$ (x = 0, 3, 6, 9) ceramics.

with increment of HfO_2 quantity, when the revised k at room temperature displays the opposite HfO_2 composition dependence. HfO_2 alloying effect enhances inharmonic lattice vibration strength and drops thermal conductivity. Figure 8(a) displays that the same amounts of Ta^{5+} and Ho^{3+} ions are substituted by Hf^{4+} cations. As the ionic radius of two Hf^{4+} cations is equal to the sum of one Ho^{3+} ion and one Ta^{5+} ion, no crystal structure expansion or shrinkage is triggered. Figure 8(b) displays that Hf^{4+} cations occupying Ta^{5+} ionic positions are the most violent phonon scattering sources because of the cage-like tetrahedron and the distinction of ionic radius between Ta and Hf. Phonons can be scattered by Hf^{4+} ions to block phonon transportation and result in low thermal conductivity.

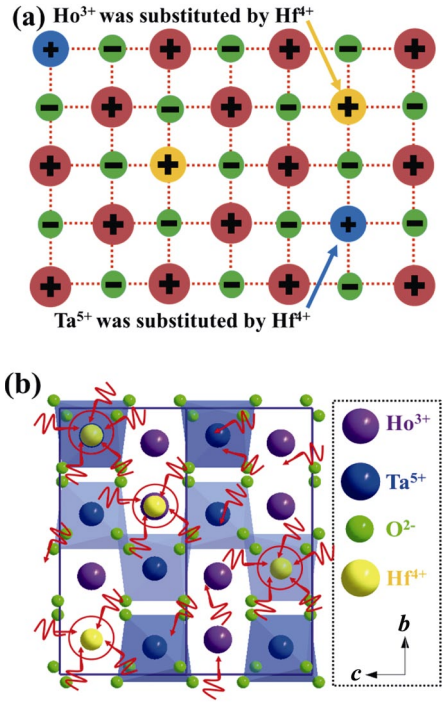

Fig. 8 Schematic drawings of 6 mol%-HfO_2 $HoTaO_4$ ceramics: (a) the same numbers of Ta^{5+} and Ho^{3+} ions are substituted by Hf^{4+}cations; (b) the phonon scattering principle diagram in 1×1×2 crystal structure.

4 Conclusions

HfO_2 alloying effect is successfully employed to decrease thermal conductivity of $HoTaO_4$ ceramics. HfO_2 alloying content in $HoTaO_4$ is higher than 6 mol% and is less than 9 mol%, and no crystal structural transition is triggered. The porosity of $HoTaO_4$ can be regulated by controlling HfO_2 quantity. The wide band gap (~5.0 eV) proves that heat is conducted by phonons in these ceramics. HfO_2 alloying effect is effective in improving thermal insulation performance of $HoTaO_4$ via enhancing inharmonic lattice vibration, introducing point defects and pores. The least thermal conductivity is 0.8 $W \cdot K^{-1} \cdot m^{-1}$ (900 ℃), which is much lower than that of other TBCs. Current document stresses that HfO_2 alloying $HoTaO_4$ ceramics are promising TBCs, contributed to the extremely low thermal conductivity.

Acknowledgements

This research is under the support of the National Natural Science Foundation of China (No. 51762028) and Materials Genome Engineering of Rare and Precious Metal of Yunnan Province (No. 2018ZE019).

References

[1] Padture NP, Gell M, Jordan EH. Thermal barrier coatings for gas-turbine engine applications. *Science* 2002, **296**: 280–284.

[2] Padture NP. Advanced structural ceramics in aerospace propulsion. *Nat Mater* 2016, **15**: 804–809.

[3] Zhang WW, Li GR, Zhang Q, *et al*. Comprehensive damage evaluation of localized spallation of thermal barrier coatings. *J Adv Ceram* 2017, **6**: 230–239.

[4] Clarke DR, Phillpot SR. Thermal barrier coating materials. *Mater Today* 2005, **8**: 22–29.

[5] Liu B, Liu YC, Zhu CH, *et al*. Advances on strategies for searching for next generation thermal barrier coating materials. *J Mater Sci Technol* 2019, **35**: 833–851.

[6] Chen L, Yang GJ. Epitaxial growth and cracking of highly tough 7YSZ splats by thermal spray technology. *J Adv Ceram* 2018, **7**: 17–29.

[7] Cao X, Vassen R, Fischer W, *et al*. Lanthanum–cerium oxide as a thermal barrier-coating material for high-temperature applications. *Adv Mater* 2003, **15**: 1438–1442.

[8] Liu B, Wang JY, Li FZ, *et al*. Theoretical elastic stiffness, structural stability and thermal conductivity of $La_2T_2O_7$ (T = Ge, Ti, Sn, Zr, Hf) pyrochlore. *Acta Mater* 2010, **58**: 4369–4377.

[9] Clarke DR. Materials selection guidelines for low thermal conductivity thermal barrier coatings. *Surf Coat Technol* 2003, **163–164**: 67–74.

[10] Zhao M, Pan W. Effect of lattice defects on thermal conductivity of Ti-doped, Y_2O_3-stabilized ZrO_2. *Acta Mater* 2013, **61**: 5496–5503.

[11] Winter MR, Clarke DR. Thermal conductivity of yttria-stabilized zirconia–hafnia solid solutions. *Acta Mater* 2006, **54**: 5051–5059.

[12] Van Sluytman JS, Krämer S, Tolpygo VK, *et al*. Microstructure evolution of ZrO_2–$YbTaO_4$ thermal barrier coatings. *Acta Mater* 2015, **96**: 133–142.

[13] Mercer C, Williams J, Clarke D, *et al*. On a ferroelastic mechanism governing the toughness of metastable tetragonal-prime (t') yttria-stabilized zirconia. *Proc R Soc A* 2007, **463**: 1393–1408.

[14] Panthi D, Hedayat N, Du YH. Densification behavior of yttria-stabilized zirconia powders for solid oxide fuel cell electrolytes. *J Adv Ceram* 2018, **7**: 325–335.

[15] Li GR, Yang GJ. Understanding of degradation-resistant behavior of nanostructured thermal barrier coatings with bimodal structure. *J Mater Sci Technol* 2019, **35**: 231–238.

[16] Wang J, Chong XY, Zhou R, *et al*. Microstructure and thermal properties of $RETaO_4$ (RE = Nd, Eu, Gd, Dy, Er, Yb, Lu) as promising thermal barrier coating materials. *Scripta Mater* 2017, **126**: 24–28.

[17] Limarga AM, Shian S, Leckie RM, *et al*. Thermal conductivity of single- and multi-phase compositions in the ZrO_2–Y_2O_3–Ta_2O_5 system. *J Eur Ceram Soc* 2014, **34**: 3085–3094.

[18] Chen L, Hu MY, Wu P, *et al*. Thermal expansion performance and intrinsic lattice thermal conductivity of ferroelastic $RETaO_4$ ceramics. *J Am Ceram Soc* 2019, **102**: 4809–4821.

[19] Chen L, Song P, Feng J. Influence of ZrO_2 alloying effect on the thermophysical properties of fluorite-type Eu_3TaO_7 ceramics. *Scripta Mater* 2018, **152**: 117–121.

[20] Liu B, Wang JY, Zhou YC, *et al*. Theoretical elastic stiffness, structure stability and thermal conductivity of $La_2Zr_2O_7$ pyrochlore. *Acta Mater* 2007, **55**: 2949–2957.

[21] Yang J, Wan CL, Zhao M, *et al*. Effective blocking of radiative thermal conductivity in $La_2Zr_2O_7$/$LaPO_4$ composites for high temperature thermal insulation applications. *J Eur Ceram Soc* 2016, **36**: 3809–3814.

[22] Wang ZJ, Zhou GH, Jiang DY, *et al*. Recent development of $A_2B_2O_7$ system transparent ceramics. *J Adv Ceram* 2018, **7**: 289–306.

[23] Li GR, Wang LS, Yang GJ. A novel composite-layered coating enabling self-enhancing thermal barrier performance. *Scripta Mater* 2019, **163**: 142–147.

[24] Chen L, Wu P, Feng J. Optimization thermophysical properties of TiO_2 alloying Sm_3TaO_7 ceramics as promising thermal barrier coatings. *Int J Appl Ceram Technol* 2019, **16**: 230–242.

[25] Wu FS, Wu P, Chen L, *et al*. Structure and thermal properties of Al_2O_3-doped Gd_3TaO_7 as potential thermal barrier coating. *J Eur Ceram Soc* 2019, **39**: 2210–2214.

[26] Christy AA, Kvalheim OM, Velapoldi RA. Quantitative analysis in diffuse reflectance spectrometry: A modified Kubelka–Munk equation. *Vib Spectrosc* 1995, **9**: 19–27.

[27] Schlichting KW, Padture NP, Klemens PG. Thermal conductivity of dense and porous yttria-stabilized zirconia. *J Mater Sci* 2001, **36**: 3003–3010.

[28] Leitner J, Chuchvalec P, Sedmidubský D, *et al*. Estimation of heat capacities of solid mixed oxides. *Thermochim Acta* 2002, **395**: 27–46.

[29] Qu ZX, Wan CL, Pan W. Thermal expansion and defect chemistry of MgO-doped $Sm_2Zr_2O_7$. *Chem Mater* 2007, **19**: 4913–4918.

[30] Ivanova OP, Naumkin AV, Vasilyev LA. An XPS study of compositional changes induced by argon ion bombardment of the $LaPO_4$ surface. *Vacuum* 1996, **47**: 67–71.

[31] Zhang XF, Zhou KS, Deng CM, *et al*. Gas-deposition mechanisms of 7YSZ coating based on plasma spray-physical vapor deposition. *J Eur Ceram Soc* 2016, **36**: 697–703.

[32] Li GR, Wang LS. Durable TBCs with self-enhanced thermal insulation based on co-design on macro- and microstructure. *Appl Surf Sci* 2019, **483**: 472–480.

[33] Ryan JL, Jørgensen CK. Absorption spectra of octahedral lanthanide hexahalides. *J Phys Chem* 1966, **70**: 2845–2857.

[34] Liu YC, Liu B, Xiang HM, *et al*. Theoretical investigation of anisotropic mechanical and thermal properties of ABO_3 (A = Sr, Ba; B = Ti, Zr, Hf) perovskites. *J Am Ceram Soc* 2018, **101**: 3527–3540.

[35] Xiang HM, Feng ZH, Li ZP, *et al*. Crystal structure, mechanical and thermal properties of $Yb_4Al_2O_9$: A combination of experimental and theoretical investigations. *J Eur Ceram Soc* 2017, **37**: 2491–2499.

[36] Wan CL, Zhang W, Wang YF, *et al*. Glass-like thermal conductivity in ytterbium-doped lanthanum zirconate pyrochlore. *Acta Mater* 2010, **58**: 6166–6172.

[37] Bruls R, Hintzen H, Metselaar R. A new estimation method for the intrinsic thermal conductivity of nonmetallic compounds: A case study for $MgSiN_2$, AlN and β-Si_3N_4 ceramics. *J Eur Ceram Soc* 2005, **25**: 767–779.

[38] Ge ZH, Ji YH, Qiu Y, *et al*. Enhanced thermoelectric properties of bismuth telluride bulk achieved by telluride-spilling during the spark plasma sintering process. *Scripta Mater* 2018, **143**: 90–93.

[39] Klemens PG. Thermal resistance due to point defects at high temperatures. *Phys Rev* 1960, **119**: 507.

[40] Ambegaokar V. Thermal resistance due to isotopes at high temperatures. *Phys Rev* 1959, **114**: 488.